LANGMUIR

Article

pubs.acs.org/Langmuir

Hollow Au−Cu_2O Core−Shell Nanoparticles with Geometry-Dependent Optical Properties as Efficient Plasmonic Photocatalysts under Visible Light

Biao Lu,[†] Aiping Liu,*[,†,‡] Huaping Wu,[§] Qiuping Shen,[†] Tingyu Zhao,[†] and Jianshan Wang[∥]

[†]Center for Optoelectronics Materials and Devices, Zhejiang Sci-Tech University, Hangzhou 310018, China

[‡]State Key Laboratory of Nonlinear Mechanics, Institute of Mechanics, Chinese Academy of Sciences, Beijing 100190, China

[§]Ministry of Education & Zhejiang Province, Key Laboratory of E&M, Zhejiang University of Technology, Hangzhou 310014, China

[∥]Tianjin Key Laboratory of Modern Engineering Mechanics, Department of Mechanics, Tianjin University, Tianjin 300072, China

Supporting Information

ABSTRACT: Hollow Au−Cu_2O core−shell nanoparticles were synthesized by using hollow gold nanoparticles (HGNs) as the plasmon-tailorable cores to direct epitaxial growth of Cu_2O nanoshells. The effective geometry control of hollow Au−Cu_2O core−shell nanoparticles was achieved through adjusting the HGN core sizes, Cu_2O shell thicknesses, and morphologies related to structure-directing agents. The morphology-dependent plasmonic band red-shifts across the visible and near-infrared spectral regions were observed from experimental extinction spectra and theoretical simulation based on the finite-difference time-domain method. Moreover, the hollow Au−Cu_2O core−shell nanoparticles with synergistic optical properties exhibited higher photocatalytic performance in the photodegradation of methyl orange when compared to pristine Cu_2O and solid Au−Cu_2O core−shell nanoparticles under visible-light irradiation due to the efficient photoinduced charge separation, which could mainly be attributed to the Schottky barrier and plasmon-induced resonant energy transfer. Such optical tunability achieved through the hollow cores and structure-directed shells is of benefit to the performance optimization of metal−semiconductor nanoparticles for photonic, electronic, and photocatalytic applications.

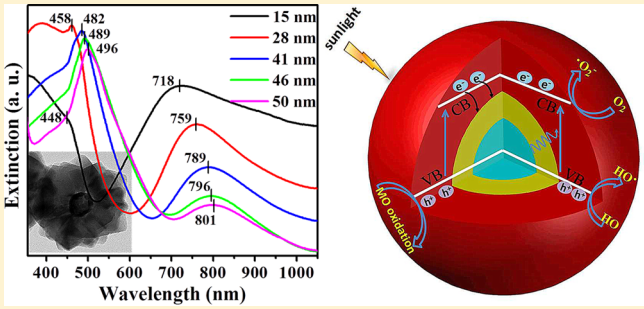

1. INTRODUCTION

Metal−semiconductor core−shell nanoparticles, which may possess the independent properties of each component as well as new synergistic and tunable properties due to the metal−semiconductor interactions,[1−14] have been given great attention due to a series of unique functionalities such as optical,[15−22] electric,[23,24] optoelectronic,[10,25−27] and catalytic properties.[28−40] By coating a semiconductor component on a metallic nanostructure, the plasmonic features of the metal, especially fascinating localized surface plasmon resonance (LSPR), can be enhanced through plasmon−exciton coupling or local dielectric environment alteration, resulting in a series of interesting optical phenomena including the enhanced optical absorption and scattering and reinforced plasmonic tunability over a broad wavelength range.[8,17,33,41,42] Furthermore, for plasmonic metal−semiconductor photocatalysts, the photocatalytic activity over an extended wavelength range for the photoresponsive semiconductor may be significantly improved due to the increasing light-harvesting and charge-separating efficiency at the metal−semiconductor interfaces either via the direct electron transfer (DET) or via the plasmon-induced resonant energy transfer (PIRET).[29,33] Since the synergistic properties of core−shell nanoparticles are sensitively dependent upon hybrid component and morphology, many efforts are carried out to precisely control both geometries and components of the hybrids to achieve highly tunable properties.[43−50] For example, the solid Au−Cu_2O core−shell nanoparticles not only combine the unique optical, electronic, and photocatalytic properties of Cu_2O nanoshells and the geometry-dependent plasmonic properties of gold nanocores (dominated by LSPR) but also exhibit expanded plasmonic tunability as well due to the coupling between gold and Cu_2O.[41,43] Several important geometrical parameters, such as size, morphology, and crystallic structure of gold cores,[17,24,45] thickness, morphology, crystallic structure and porosity of Cu_2O shells,[4,46,47] and interior structures of the shells,[16,14,33] are systematically and selectively adjusted, resulting in synergistic photovoltaic and photocatalytic behaviors over a broad spectral range across the visible and near-infrared regions.

Compared with the solid gold nanoparticle (SGN), the hollow gold nanoparticle (HGN) has stronger plasmon resonance, wider plasmonic tuning range, and larger near-field

Received: January 29, 2016
Revised: March 7, 2016
Published: March 8, 2016

DOI: 10.1021/acs.langmuir.6b00331
Langmuir 2016, 32, 3085−3094

enhancement.[51,52] However, as far as we know, there is far less explored research related to the optical and photocatalytic tunability of HGN-based (Au−Cu_2O) core−shell nanoparticles. There is no investigation of rich structural variety of shells produced by employing HGN cores. In this paper, we report the synthesis of hollow Au−Cu_2O core−shell nanoparticles by using HGNs as the plasmon-tailorable cores to direct epitaxial growth of Cu_2O nanoshells through simple and robust wet chemistry approaches at room temperature. We demonstrate that the hollow Au−Cu_2O core−shell nanoparticles combine the SPR tunability of plasmonic HGN cores in the visible and near-infrared ranges and the photoresponsive performance of Cu_2O shells in the visible range. By changing the geometrical parameters such as the HGN core sizes and Cu_2O shell thicknesses, we can systematically adjust the optical properties of hollow hybrids over a broad spectral range across the visible and near-infrared regions. Moreover, when substituting the structure-directing agent poly(ethylene glycol) (PEG) used in the synthesis for polyvinylpyrrolidone (PVP), the geometry of hollow Au−Cu_2O core−shell nanoparticles changes from textured protrusions to quasi-spheres, resulting in the change of SPR peak. All these geometry-dependent optical properties of hollow Au−Cu_2O core−shell nanoparticles are matched well with the calculated results obtained by the finite-difference time-domain (FDTD) method. Additionally, the predominant photocatalytic activities of these hollow core−shell nanoparticles are confirmed by the degradation of methyl orange (MO) under visible-light irradiation, when compared to the pristine Cu_2O nanoparticles and solid core−shell nanoparticles. Our result is helpful for understanding the effect of core−shell interaction on the tunable plasmonic feature and interesting optical and photocatalytic performances of hybrid nanoparticles.

2. EXPERIMENTAL SECTION

2.1. Raw Materials. Chloroauric acid trihydrate ($HAuCl_4{\cdot}3H_2O$, 99%), sodium borohydride ($NaBH_4$), cobalt chloride hexahydrate ($CoCl_2{\cdot}6H_2O$), trihydrate sodium citrate (TCD, $C_6H_5Na_3O_7{\cdot}3H_2O$, purity 99%), cupric acetate ($Cu(Ac)_2{\cdot}H_2O$), ascorbic acid (AA), sodium hydroxide (NaOH), PVP (K-30), and PEG (MW =10 000) were supplied by Sigma, USA. All chemicals were of analytical grade and used without further purification. The deionized water used in the synthesis was obtained from Millipore Q purification system (resistivity >18 MΩ·cm).

2.2. Synthesis of HGNs and SGNs Colloids. The HGNs with tunable LSPR properties were synthesized by using a similar technique developed by Zhang,[53] as described in our previous report.[54] In a typical procedure, a mixture solution including 75 mL of deionized water and a certain amount of TCD (0.1 mol/L) was deoxygenated with argon gas, and then 100 μL of $CoCl_2$ (0.4 mol/L) and a certain amount of fresh $NaBH_4$ (1 mol/L) were successively injected in the above mixed solution with a prompt color change from colorless to brown in the fast reaction process due to the reduction of Co^{2+} to cobalt nanoparticles. In the case of slow reaction, 100 μL of $CoCl_2$ solution was added by dropwise with the color of the mixed solution changing to light brown when cobalt nanoparticles produced. After that, the cobalt nanoparticle colloid was fast transferred to a stirring $HAuCl_4$ solution. The HGNs were collected by centrifugation at 8500 rpm for 15 min and finally dispersed in 5 mL of deionized water. By controlling the reaction rate, the HGNs with adjustable sizes and shell thicknesses were obtained. The SGNs used as a reference were synthesized by the classic Frens' method.[54] Briefly, 1.5 mL of TCD (the mass fraction of 1%) was added quickly into the boiling solution of 100 mL of 0.25 mmol/L $HAuCl_4$ with stirring to react for 15 min. Then the solution was cooled down to the room temperature with stirring, and the SGN colloids with adjustable sizes were obtained by controlling the reaction time.

2.3. Synthesis of Hollow and Solid Au−Cu_2O Core−Shell Nanoparticles. For the synthesis of hollow Au−Cu_2O core−shell nanoparticles, 0.1 g of structure-directing agent (PEG or PVP) was completely dissolved in 8.5 mL of deionized water, followed by the addition of 0.5 mL of 0.02 mol/L $Cu(Ac)_2$ solution in a glass vial, and then 1.0 mL of concentrated HGNs colloids were injected into the glass vial with vigorous stirring. After that, 0.01 mol/L AA and 0.15 mol/L NaOH mixed solutions were added into glass vial immediately with stirring and left undisturbed for 1 h to complete the reaction. By choosing the structure-directing agent (PEG or PVP), the morphologies of hollow Au−Cu_2O core−shell nanoparticles were adjusted as well. The product was collected by centrifugation at 8000 rpm for 15 min and washed with the mixed solution of deionized water and ethanol (1:1 volume ratio) for several times to clearly remove PEG or PVP. All of the synthesis procedures were carried out at room temperature. The thickness of Cu_2O nanoshells could be tuned by varying the volumes of concentrated HGNs colloids from 0.3 to 1.8 mL in the reaction (Table 1). The solid Au−Cu_2O core−shell nanoparticles were also prepared via a similar process by using SGN as the cores. Pristine Cu_2O nanoparticles were prepared using the above-mentioned procedure without the addition of concentrated HGNs or SGNs colloids.

Table 1. Average Overall Radii (R_3) of Hollow Au−Cu_2O Core−Shell Nanoparticles Prepared with Various Volumes of Concentrated HGNs Colloids in the Reaction[a]

volume of HGNs colloids (mL)	outer radius R_2 (nm)	overall radius R_3 (nm)
1.8	17 ± 1.2	32 ± 1.5
1.0	17 ± 1.2	45 ± 2.0
0.6	17 ± 1.2	57 ± 2.2
0.4	17 ± 1.2	63 ± 2.5
0.3	17 ± 1.2	67 ± 2.8

[a]The experimental data were obtained from TEM measurements and analyzed statistically from large amounts of HGNs (at least 100 particles). The HGN575 is used as the core and the structure-directing agent is PEG.

2.4. Characterization. The morphologies and structures of nanoparticles were observed by a Field emission scanning electron microscope (FESEM, Hitachi S4800) and a transmission electron microscopy (TEM, Hitachi H-7650) at an operating voltage of 200 kV. High-resolution TEM (HRTEM) images, selected area electron diffraction (SAED) patterns, and EDS mapping images were recorded on a TEM (FEI Tecnai G2 F30 S-Twin, USA) working at 300 kV. The crystalline structures of nanoparticles were obtained on a X-ray diffractometer (Bruker AXS D8) using the Cu Kα radiation (λ = 0.154 18 nm) with the 2θ scan from 10° to 80° at a step of 0.02°. The optical properties of nanoparticles were taken by a Hitachi U-3900 UV−vis spectrophotometer at room temperature.

For photocatalytic properties measurement, 4 mg of photocatalyst was dispersed into 80 mL of 15 mg/L MO solution at room temperature. Prior to irradiation, the suspension was magnetically stirred for 1 h in dark to ensure reach an adsorption/desorption equilibrium between the photocatalysts and MO. A 300 W xenon lamp equipped with a UV cutoff filter (λ > 400 nm) was used as the light source, which was placed 12 cm away from the solution. Then the solution was exposed to light irradiation under magnetic stirring with circular water-cooling system to guarantee the solution at room temperature. At every 30 min of irradiation, 6 mL of sample solution was drawn from the system and centrifuged to remove the photocatalysts to analyze MO concentration using a Hitachi U-3900 UV−vis spectrophotometer. The characteristic absorption of MO at 464 nm was used to evaluate the photocatalytic activities of photocatalysts. The degradation percentage was calculated by measuring the absorption of MO solution at each irradiation time

DOI: 10.1021/acs.langmuir.6b00331
Langmuir 2016, 32, 3085−3094

interval (C) and the absorption of the initial concentration (C_0) at adsorption−desorption equilibrium.

2.5. Reactive Species Trapping Experiments. To investigate the reactive species involved in the photocatalytic experiments and clarify the contribution of different reactive species, 2 mmol/L different scavengers, such as triethanolamine (TEOA) as h^+ scavenger, isopropanol (IPA) as ·OH scavenger and *p*-benzoquinone (PBQ) as $\cdot O_2^-$ scavenger, were added into the MO solution, respectively, and the changes of MO absorption spectra were measured after irradiation for 1 h.

2.6. Finite-Difference Time-Domain (FDTD) Calculation. The extinction spectra of hollow Au−Cu_2O core−shell nanoparticles were calculated by the FDTD solution (Lumerical, Canada). The geometry of the nanoparticles was assumed to be a concentric three-layered sphere with the cross-sectional drawing shown in Figure 1A. The inner layer with the inner radius (R_1) was supposed to be water with the refractive index of 1.33. The interlayer (radius R_2) and the outer layer (radius R_3) were assumed to be gold and Cu_2O layers, respectively. The wavelength-dependent empirical dielectric functions of bulk gold and Cu_2O were extracted from Palik and Johnson Christy databases, respectively.[55,56] Calculations were done for isolated Au−Cu_2O core−shell nanoparticle in water (refractive index of 1.33) and excited by linearly polarized light. The geometrical parameters were obtained based on the statistical analysis from large amounts of Au−Cu_2O core−shell nanoparticles (at least 100 particles) on random ten TEM images.

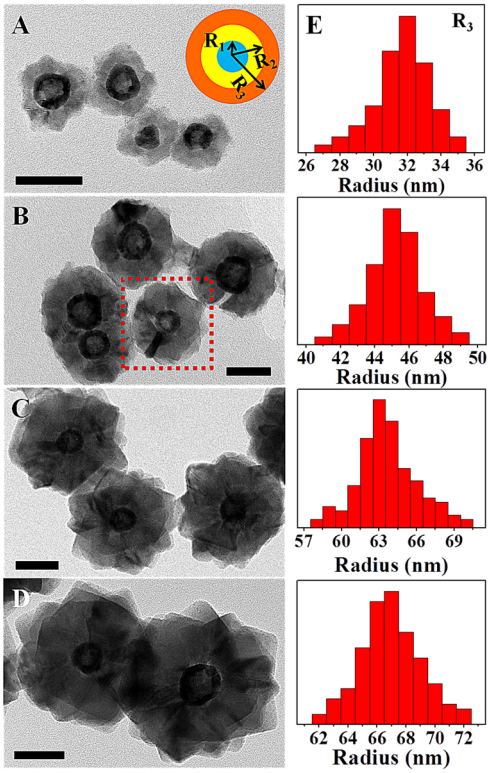

Figure 1. TEM images of hollow Au−Cu_2O core−shell nanoparticles with tunable thicknesses of Cu_2O shells by adding different volumes of HGNs colloids in the reaction: (A) 1.8, (B) 1.0, (C) 0.4, and (D) 0.3 mL. All of TEM images have the same scale bar of 50 nm. The scheme of cross-sectional drawing of hollow Au−Cu_2O core−shell nanoparticle is shown in (A). R_1, R_2, and R_3 are the average inner radius and outer radius of given HGNs and overall radius of given Au−Cu_2O core−shell nanoparticles, respectively. (E) Size distribution histograms (R_3) of the aforementioned Au−Cu_2O core−shell nanoparticles with different thicknesses of Cu_2O shells. The HGN575 is used as the core, and the structure-directing agent is PEG.

3. RESULTS AND DISCUSSION

3.1. Structural Characterization of Hollow Au−Cu_2O Core−Shell Nanoparticles. We recently reported geometry-dependent plasmonic optical properties of HGNs.[54] Here we synthesize HGNs with four different sizes and SGNs with two sizes. The extinction spectra and corresponding photographs of nanoparticle colloids, TEM images, and size distribution histograms of nanoparticles are shown in Figures S1 and S2. We name the HGNs and SGNs samples with the position of SPR peaks at the extinction spectra in the following discussion. The TEM images of dispersed HGNs with different sizes in Figure S1 show a strong contrast difference in all of the HGNs with a bright interior cavity and a dark shell, which confirms their hollow architectures.[54] The average outer radius (R_2) and inner radius (R_1) of HGNs which are measured and analyzed statistically from a large amount of HGNs (at least 100 particles) are 9 ± 1.0 nm and 5 ± 0.8 nm for HGN545, 17 ± 1.2 nm and 9 ± 1.0 nm for HGN575, 22 ± 2.0 nm and 12 ± 1.5 nm for HGN596, and 33 ± 2.5 nm and 18 ± 2.0 nm for HGN633, respectively. Therefore, all HGNs have a similar aspect ratio (inner diameter/outer diameter) near 0.55. The narrow single Gaussian distributions of HGN sizes indicate that the samples are highly monodisperse with size distribution within 9.5% standard deviation. Comparably, the sizes of ellipsoidal SGN522 are 20 ± 1.5 nm in the major axis and 17 ± 1.5 nm in the minor axis, while SGN528 are 34 ± 2.0 nm in the major axis and 28 ± 2.0 nm in the minor axis (Figure S2). Additionally, the HGNs present wide plasmonic tuning range with the SPR band position altered over a wavelength region from 545 to 633 nm when the color of colloidal HGNs changes from red to purple and to green. When consideration the similar increase in size (16 nm from HGN545 to HGN575 and 14 nm from SGN522 to SGN528), the HGNs give a 30 nm red-shift of SPR band position compared to just 6 nm one for SGHs. This makes HGNs superior in optical tunability and possible photocatalyst application.

When the metal core is coated by a semiconductor, the direct epitaxial overgrowth of monocrystalline semiconductor nanoshells on the surface of highly faceted or quasi-spherical metallic nanoparticle cores has been reported even large lattice mismatch existence.[13,57,58] In our study, the epitaxial growth of Cu_2O on the HGNs surface is of possibility because of the similar crystal symmetry of Cu_2O to gold and good affinity to gold surface. Figures 1A−D show typical TEM images of hollow Au−Cu_2O core−shell nanoparticles with increasing shell thicknesses (HGN575 core, PEG as the structure-directing agent). It apparently reveals that each individual core−shell nanoparticle with obvious core−shell contrast has a HGN in the center and dense Cu_2O shell coated on the fringe to form concentric nanostructure. The thickness of Cu_2O shell increases from 15 ± 1.2 to 50 ± 2.0 nm with the volume decrease of concentrated HGNs colloids from 1.8 to 0.3 mL in the reaction (Table 1). The shell becomes rougher with nanoscaled protrusions when the thickness of Cu_2O shell progressively increases (also see Figure 2A). Figure 1E shows the size distribution histograms (overall radius R_3) of the above-mentioned four Au−Cu_2O core−shell nanoparticles by statistical measurement and analysis from large amounts of hollow Au−Cu_2O core−shell nanoparticles. All particles have a size distribution approaching to narrow single Gaussian peak, and the corresponding average R_3 determined from the mean value of Gaussian distribution is 32 ± 1.5, 45 ± 2.0, 63 ± 2.5,

DOI: 10.1021/acs.langmuir.6b00331
Langmuir 2016, 32, 3085−3094

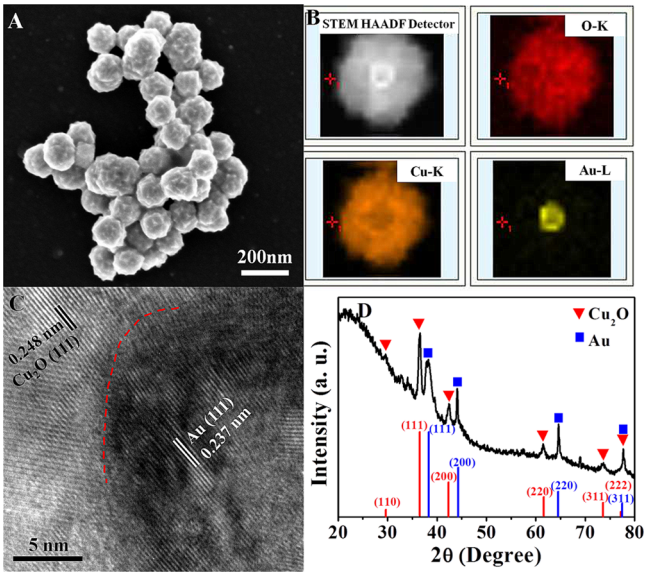

Figure 2. (A) SEM image of hollow Au−Cu_2O core−shell nanoparticles in Figure 1D. (B) EDS mapping images of individual Au−Cu_2O core−shell nanoparticle in Figure 1B. (C) HRTEM image of individual Au−Cu_2O core−shell nanoparticle in Figure 1A. (D) XRD pattern of hollow Au−Cu_2O core−shell nanoparticles. Red lines and blue lines present the standard diffraction data of face-centered cubic crystalline Cu_2O and gold, respectively. The HGN575 is used as the core, and the structure-directing agent is PEG.

and 67 ± 2.8 nm, which correspond to average Cu_2O shell thickness of 15 ± 1.2, 28 ± 1.2, 46 ± 1.5, and 50 ± 2.0 nm, respectively. Figure 2B shows the elemental mapping images of an individual core−shell nanoparticle, which clearly displays the presence of Au, Cu, and O elements. The Au signals are strictly confined in the central region of the particle where the gold core is located, while the Cu and O elements are distributed over the whole cross section of core−shell particle. Since no pristine and single Cu_2O particles are observed in all of TEM images, we could speculate on the mechanism of heterogeneous nucleation which controls the overgrowth of hollow Au−Cu_2O core−shell nanoparticles.

To clearly characterize the core−shell interfacial structures and to interpret the growth mechanism, the HRTEM image of individual Au−Cu_2O core−shell nanoparticle with thin shell (Figure 1A) is shown in Figure 2C. The lattice fringes of gold on the interface present a Au−Au spacing of 0.237 nm, which corresponds to the (111) planes of gold, while the lattice fringes of Cu_2O on the interface present a Cu−Cu spacing of 0.248 nm, corresponding to the (111) planes of Cu_2O. This is to say the (111) planes of Cu_2O grow epitaxially on the {111} facets of gold. The interfacial lattice mismatch is about 4.6%, which is close to the reported 4.5% for solid Au−Cu_2O core−shell structures.[4] The XRD pattern shown in Figure 2D clearly indicates that both gold and Cu_2O in as-fabricated core−shell nanoparticles have diffraction peaks of (111), (200), (220), and (311) planes, corresponding to pure cubic-phase gold (JCPDS, 5-667) and Cu_2O (JCPDS, 65-3288). It is worth noting that the nanoscaled protrusions are prominent for thick Cu_2O shells. To explore the formation mechanism of protrusions, we prepared pristine Cu_2O nanoparticles by similar procedures without adding HGNs colloids. Typical SEM and TEM images in Figure S3 reveal the pure Cu_2O truncated nanocubes with average size of 40 ± 5.0 nm by using PEG as structure-directing agent. The XRD pattern in Figure S3C shows the as-prepared production is pure face-centered cubic crystalline Cu_2O (JCPDS, 65-3288) without any impurities. Therefore, we infer that the Cu_2O nanoparticles are primitively heterogeneous nucleated and deposited on the surface of HGNs by local epitaxial growth. The protrusions actually results from the multiple Cu_2O cubes which are trying to form on the same HGN core. Analogously, the morphology and microstructure of solid Au−Cu_2O core−shell nanoparticles (SGN528 core, PEG as structure-directing agent) are confirmed by SEM, TEM, and XRD analyses (Figure S4).

When substituting the structure-directing agent PEG with PVP, we find that the surface morphologies of hollow Au−Cu_2O core−shell nanoparticles dramatically change, as shown in Figure 3. The thickness of Cu_2O shells can also be precisely controlled from 20 to 50 nm just via simply adjustion of the volume of concentrated HGN596 colloids from 1.8 to 0.3 mL in the reaction (Figure 3B and Figure S5A). The HRTEM image of interface between HGN core and Cu_2O shell indicates the (111) planes of Cu_2O grow epitaxially on the {111} facets of gold (Figure 3C) with the interfacial lattice mismatch about 4.7%. The monocrystalline domains with different orientations for Cu_2O nanoparticles indicate that the Cu_2O shell has a polycrystalline structure. The XRD pattern of the sample in Figure S5B indicates that the core−shell nanoparticles are composed of pure cubic-phase Au (JCPDS, 5-667) and Cu_2O (JCPDS, 65-3288). Notice that the hollow Au−Cu_2O core−shell nanoparticles prepared by using PVP structure-directing agent keep quasi-spherical shape even the HGNs colloids are very scarce in the reaction. The pristine Cu_2O nanoparticles prepared by similar procedures without adding HGNs colloids are also quasi-spherical shape with broad distributions of particle sizes due to the heterogeneous nucleation process (Figure S6A). The diffraction rings from inside to outside in SAED pattern (Figure S6B) correspond to the (111), (200), (220), and (311) planes of pure face-centered cubic crystalline

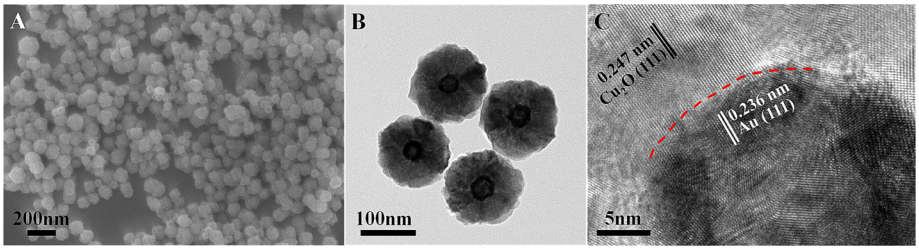

Figure 3. (A) SEM, (B) TEM, and (C) HRTEM images of hollow Au−Cu_2O core−shell nanoparticles with tunable thicknesses of Cu_2O shells by adding different volumes of HGNs colloids in the reaction: (A, B) Cu_2O shell thickness about 50 nm by adding 0.3 mL of HGN596 colloids in the reaction; (C) Cu_2O shell thickness about 20 nm by adding 1.8 mL of HGN596 colloids in the reaction. The structure-directing agent is PVP.

DOI: 10.1021/acs.langmuir.6b00331
Langmuir 2016, 32, 3085−3094

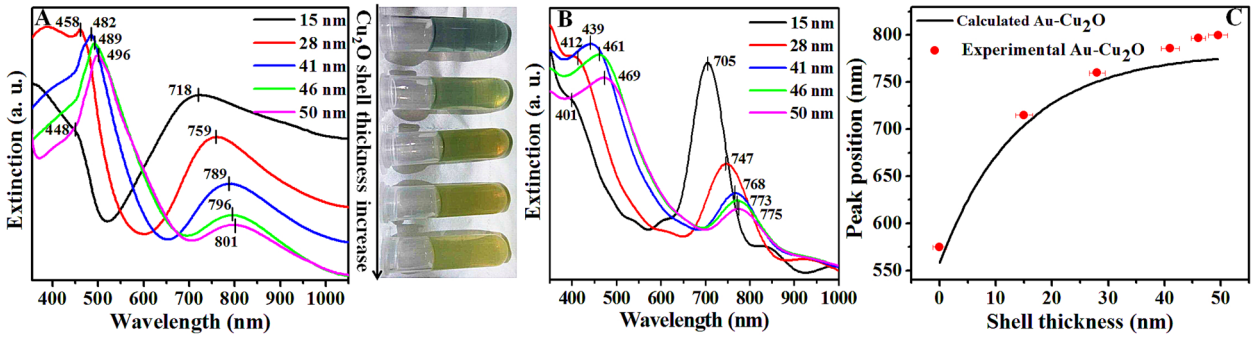

Figure 4. (A) Experimental extinction spectra of hollow Au−Cu_2O core−shell nanoparticles and corresponding photographs of Au−Cu_2O colloids with increasing Cu_2O thickness in the range from 15 to 50 nm (from top to bottom) by adding different volumes of HGNs colloids in the reaction. The overall radius R_3 of Au−Cu_2O core−shell nanoparticles are 32 ± 1.5, 45 ± 2.0, 57 ± 2.2, 63 ± 2.5, and 67 ± 2.8 nm (from top to bottom). HGN575 is used as the core and the structure-directing agent is PEG. (B) Calculated extinction spectra of hollow Au−Cu_2O core−shell nanoparticles with similar geometrical parameters as (A). The inner radius R_1 and outer radius R_2 of HGNs are fixed at 9.0 and 17.0 nm; the overall radius R_3 of Au−Cu_2O core−shell nanoparticles are 32, 45, 57, 63, and 67 nm (from top to bottom). The filling medium in the hollow part and surrounding medium outside the Au−Cu_2O core−shell nanoparticles is H_2O. (C) Experimentally measured and calculated plasmon resonance wavelengths as a function of Cu_2O shell thickness. The error bars for the experimental data points show the standard deviation determined by TEM measurements over 100 particles for each sample.

Cu_2O, respectively, which is consistent with the XRD pattern in Figure S6C. It implies that the surfaces of HGN cores composed of atomically well-defined crystalline facets can serve as the locally flat substrates for the epitaxial growth of Cu_2O nanoparticles to form polycrystalline cubic-phase nanoshells by using PVP as structure-directing agent. Wang et al. reported that random-oriented Cu_2O nanocrystallites could hierarchically self-assemble into a mesoscopic spherical particle on the surface of gold core to form a polycrystalline Cu_2O nanoshell in the presence of PVP structure-directing agent.[43]

3.2. Geometry-Dependent Optical Properties of Hollow Au−Cu_2O Nanoparticles. The geometry-dependent optical properties of hollow Au−Cu_2O nanoparticles are studied via the UV−vis absorption spectra through adjusting the HGN core sizes, Cu_2O shell thicknesses, and morphologies related to structure-directing agents. Figure 4A displays the experimental extinction spectra of as-prepared hollow Au−Cu_2O core−shell nanoparticles with fixed HGN575 core and increasing shell thickness of Cu_2O. The Au−Cu_2O core−shell nanoparticles exhibit highly tunable optical properties with the broad SPR spectra spanning the visible and near-infrared regions. Compared to the extinction spectra of pristine HGNs colloids (Figure S1B) and Cu_2O truncated nanocubes (Figure S7A), the experimental extinction spectra of hollow Au−Cu_2O core−shell nanoparticles are more complicated. The extinction at wavelength range below 560 nm is determined by the strong excitation interband transition of Cu_2O shell,[43] which is in accordance with extinction spectrum of pure Cu_2O truncated nanocubes (Figure S7A). With the increase of overall radius R_3 of hollow core−shell nanoparticles, the multipeaked line shapes and red-shift of peaks at wavelength range below 560 nm are primarily arising from geometry-dependent optical properties of Cu_2O shell.[43] The spectral features at the wavelength range above 600 nm could be assigned to the plasmon resonances of HGN cores, whose frequencies red-shift from 575 nm for bare HGNs colloids (Figure S1B) to 718 nm due to the couple between Cu_2O and HGN (Figure 4A). The obvious red-shift of SPR peak of HGN is primarily due to the high refractive index of Cu_2O ($n \approx 2.7$) surrounding HGN core. Since the n is related to permittivity ε via $\varepsilon = n^2$,[49] this plasmon resonance frequency is sensitively dependent on the thickness of Cu_2O shells and progressively shifts to larger wavelengths (801 nm) with the increasing of Cu_2O shell thickness. It is apparent that the extinction spectra of these core−shell nanoparticles are not a simple linear combination of the optical features of HGNs and Cu_2O components but a synergistic effect with expanded and red-shifted SPR peaks from visible into near-infrared range. The Au−Cu_2O interactions also result in the color change of hybrid colloids from blue-green to yellow-green and to yellow during the progressive increase of shell thickness (Figure 4A). By contrast, we prepared solid Au−Cu_2O core−shell nanoparticles with SGN528 as the core (SGN528 has a similar size to HGN575). Though the plasmon resonance peak of the solid nanoparticles reds shift with the increase of Cu_2O thickness, the expanded region is relative narrower than that of hollow ones (Figure S8), indicating the inferior tunable optical properties of solid system. The controllable shell thickness of Cu_2O is also achieved by using different sized HGN cores. Their corresponding hollow Au−Cu_2O core−shell nanoparticles exhibit highly tunable optical properties with obvious red-shifts for the interband transition peaks of Cu_2O shells and SPR peaks of HGN cores during the progressive increase of shell thickness (Figure S9). Therefore, by controlling the sizes of HGN cores and the thicknesses of Cu_2O shells, the hollow Au−Cu_2O core−shell nanoparticles exhibit geometry-dependent optical properties with the broad SPR spectra spanning the visible and near-infrared regions.

To understand the optical features better, we adopted the FDTD method to calculate the extinction spectra of the hollow Au−Cu_2O core−shell nanoparticles by using the model of concentrically and spherically symmetric three-layered particle with geometrical parameters and compositions matching the experimentally fabricated nanoparticles. The dielectric medium filling the hollow part and surrounding the outer surface of the particles is water (n = 1.33). As shown in Figure 4B, the calculated extinction spectra present multipeaked spectral features in the visible and near-infrared range with progressive red-shift as the thickness increase of Cu_2O shells. The overall line shapes in the calculated extinction spectra match the experimental ones reasonably well, while the experimental extinction spectra exhibit larger spectral shifts and broader bandwidths than the calculated ones due to the structural

DOI: 10.1021/acs.langmuir.6b00331
Langmuir 2016, 32, 3085−3094

nonideality and polydispersity of both HGN cores and Cu_2O shells. The shell thickness-dependent evolution of peak position can be interpreted in the context of the high refractive index of Cu_2O and geometry-dependent couple between Cu_2O and gold.[43] This deviation between the experimental peak position with that of calculated one increases with the increase of shell thickness, which might be ascribed to the surface roughness of shells with nanoscaled protrusions.

Furthermore, the morphology of Cu_2O shells adjusted by the structure-directing agents also affects the SPR band position of hollow Au−Cu_2O core−shell nanoparticles. As depicted in Figure 5A, the hollow Au−Cu_2O core−shell nanoparticles with

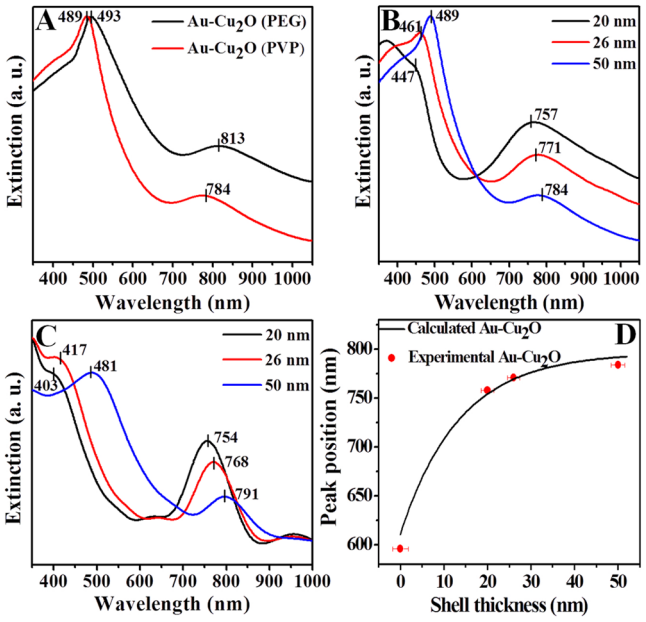

Figure 5. (A) Experimental extinction spectra of hollow Au−Cu_2O core−shell nanoparticles with similar geometrical parameters (HGN596 core, Cu_2O thickness of 50 nm) by using the structure-directing agents of PEG and PVP. (B) Experimental extinction spectra of hollow Au−Cu_2O core−shell nanoparticles with increasing Cu_2O thickness in the range from 20 to 50 nm (from top to bottom) by adding different volumes of HGNs colloids in the reaction. The overall radius R_3 of Au−Cu_2O core−shell nanoparticles are 42 ± 2.0, 48 ± 2.2, and 72 ± 3.0 nm (from top to bottom). HGN596 is used as the core and the structure-directing agent is PVP. (C) Calculated extinction spectra of hollow Au−Cu_2O core−shell nanoparticles with similar geometrical parameters as (B). The inner radius R_1 and outer radius R_2 of HGNs are fixed at 12 and 22 nm; the overall radius R_3 of Au−Cu_2O core−shell nanoparticles are 42, 48, and 72 nm (from top to bottom). The filling medium in the hollow part and surrounding medium outside the Au−Cu_2O core−shell nanoparticles is H_2O. (D) Experimentally measured and calculated plasmon resonance wavelengths as a function of Cu_2O shell thickness. The error bars for the experimental data points show the standard deviation determined by TEM measurements over 100 particles for each sample.

identical HGN596 cores and similar thicknesses of Cu_2O shells (~50 nm) present discrepant extinction spectra just changing the structure-directing agent from PEG to PVP. The red-shift of SPR peak is more apparent for PEG system. It is suggested that the relative intensity ratio of scattering spectra to absorption spectra might be enhanced by the rougher Cu_2O shell with nanoscaled protrusions when the core−shell particle size increases.[4,17] Since the SPR peaks in scattering spectra are closer to long wavelength region relative to the ones in absorption spectra,[17] the SPR peak position of hollow Au−Cu_2O core−shell nanoparticles prepared with PEG is of larger wavenumber compared to that of Au−Cu_2O core−shell nanoparticles prepared with PVP. Moreover, the hollow Au−Cu_2O core−shell nanoparticles prepared by the PVP also exhibit highly tunable optical properties with obvious red-shift of SPR spectra toward higher wavelength ranges during the progressive increase of shell thickness (Figure 5B), and the FDTD method well simulates the dynamic process (Figure 5C). Compared with the results obtained by using the PEG, the experimental spectra of hollow Au−Cu_2O core−shell nanoparticles prepared by PVP are closer to the calculated results due to the quasi-spherical surface of the nanoparticles, which is approaching to the supposed calculation model. The extinction spectrum of pure Cu_2O nanospheres prepared by using the PVP is shown in Figure S7B.

3.3. Geometry-Dependent Photocatalytic Properties of Hollow Au−Cu_2O Nanoparticles. The photocatalytic activities of the hollow Au−Cu_2O core−shell nanoparticles were evaluated by the photogradation of MO under visible-light irradiation. For the choice of core size and shell thickness for photocatalysis, we should consider the following factors according to Wu's reports.[29] First, the distribution of local electromagnetic (EM) field of specific sized gold nanoparticles influences the coupling of gold and Cu_2O. Second, the spectral overlap degree of the gold LSPR with the interband absorption band of Cu_2O affects the plasmon-mediated generation of charge carriers in Cu_2O. The increasing Cu_2O shell thickness leads to a red-shift of the gold LSPR peak, changing the strength of the plasmonic energy transfer. Finally, the thickness of Cu_2O affects the lifetimes and recombination of LSPR-induced charge carriers due to the various surface states. Wu et al. analyzed the contributions of Ag LSPR and the Cu_2O interband absorption by deconvolving the UV−vis spectrum and calculated the LSPR-induced local EM field enhancement, suggesting an optimized shell thicknesses around 20−30 nm for Ag@Cu_2O core−shell photocatalysts. On the basis of this inspiration and our data of UV−vis spectra (Figure 4A and Figure S9), we speculate the hollow Au−Cu_2O nanoparticles (HGN575 core, Cu_2O thickness about 28 nm) under the current experimental conditions possess the superior photocatalytic activity. Our results of photocatalytic measurements further confirm above conclusion. Prior to irradiation, the suspension was magnetically stirred for 1 h in the dark to ensure reach an adsorption/desorption equilibrium between the photocatalysts and MO. Figure 6 shows the extinction spectra of MO solution during photocatalytic degradation for 90 min by using hollow Au−Cu_2O core−shell nanoparticles with different core sizes and Cu_2O thicknesses. There exists an optimal core size (about 34 nm) and shell thickness (about 28 nm) for maximizing the overall visible-light photocatalytic activity since the strength of plasmonic energy transfer and the resulting photocatalysis enhancement depend on the shell thickness, LSPR strength, the coupling of the near-field interaction between gold and Cu_2O, and the lifetimes of charge carriers.[29] Furthermore, under light irradiation, the absorption peak of MO at 464 nm diminishes gradually as the irradiation time increases (Figure S10). The photodegradation effect of MO is more evident by using the hollow Au−Cu_2O core−shell nanoparticles (HGN575 core, Cu_2O 28 nm), especially the one prepared by PVP, with 96% MO decolorization within 150 min (Figure 7). Since the nanoscaled protrusions of the nanoparticles prepared by PEG make the

DOI: 10.1021/acs.langmuir.6b00331
Langmuir 2016, 32, 3085−3094

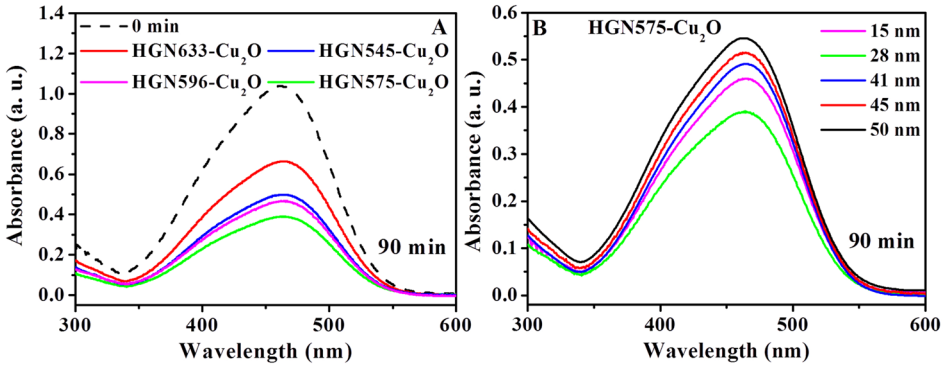

Figure 6. Variation in the extinction spectra of MO solution in the presence of different photocatalysts under visible-light irradiation for 90 min: (A) hollow Au−Cu_2O core−shell nanoparticles with different HGN cores and about 28 nm thickness Cu_2O shells; (B) hollow Au−Cu_2O core−shell nanoparticles with HGN575 cores and various thicknesses of Cu_2O shells. The structure-directing agent is PEG.

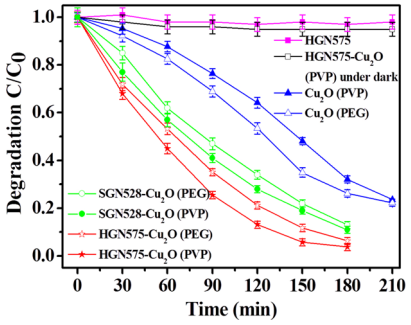

Figure 7. Photocatalytic degradation of MO as a function of irradiation time in the presence of various photocatalysts under visible-light irradiation. The HGN575 and SGN528 are used as the cores, and the Cu_2O shell thickness is about 28 nm.

SPR peaks red-shift toward larger wavelength (Figure S11), which might result in a relative low overlap area between the LSPR dipole of HGNs and interband transition dipole of Cu_2O in extinction spectra and subsequent reduction in the plasmonic energy transfer and photodegradation efficiency. The pure HGNs photocatalyst does not give rise to thermochemical degradation of MO (Figure 7) due to the possible inhibition of LSPR-mediated local heating in our system.[59] Therefore, our results indicate that the incorporation of gold cores evidently enhances the photocatalytic activity of Cu_2O shells by the efficient separation of photogenerated electrons and holes. Since photocatalysis enhancement occurs within the position of LSPR band, this indicates that the electron−hole pairs in the semiconductor can be created via the DET and/or PIRET.[33] For the DET mechanism which requires direct contact between core and shell, hot electrons transfer occurs only when plasmonic metals contact with an electron-donor solution or a hole-transporting material for keeping the charge balance.[10,28] Since no electron-donor solution or hole-transporting material exists in our reaction system, the PIRET mechanism is supposed to be dominant. Compared with solid Au−Cu_2O core−shell nanoparticles (Figure S10), the hollow Au−Cu_2O ones exhibit higher photoactivity in degradation of MO due to HGNs with similar geomorphic parameters supplying stronger plasmon resonance and near-field enhancement.[52] The corresponding normalized rate constant for the photodegradation of MO is 4.07×10^{-3}, 3.28×10^{-3}, 3.02×10^{-3}, 2.83×10^{-3}, 1.02×10^{-3}, and 1.51×10^{-3} min^{-1} mg^{-1} in the presence of HGN−Cu_2O (PVP), HGN−Cu_2O (PEG), SGN−Cu_2O (PVP), SGN−Cu_2O (PEG), Cu_2O (PVP), and Cu_2O (PEG). Besides, the stability of the HGN−Cu_2O (PVP) photocatalysts is significant and investigated by SEM, TEM, and XRD characterizations after three-cycle photocatalysis test (Figure 8). The morphology and microstructure have not

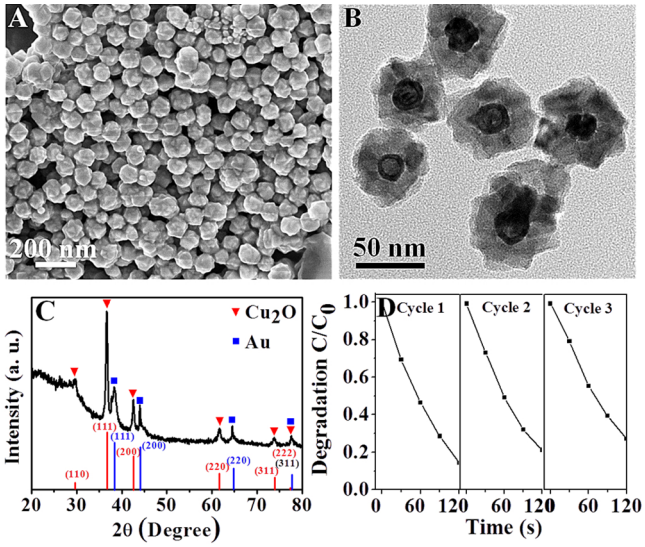

Figure 8. (A) SEM image, (B) TEM image, and (C) XRD pattern of hollow Au−Cu_2O core−shell nanoparticles after three-cycle photocatalysis tests. (D) Recyclability of hollow Au−Cu_2O core−shell nanoparticles as photocatalysts for MO photodegradation under visible light irradiation. The degradation rate C/C_0 is calculated by measuring the absorption of MO solution at each irradiation time interval (C) and the absorption of the initial concentration (C_0) at adsorption−desorption equilibrium. The HGN575 is used as the core and the thickness of Cu_2O shell is about 28 nm. The structure-directing agent is PVP.

obvious change, indicating the photocatalysts possess high stability and low photocorrosion during the photocatalytic reaction. The reusability of the photocatalysts has been confirmed by three cyclic utilization with slight decrease of catalytic activity due to the possible loss of catalysts during centrifugation.

Consideration the photodegradation of organic pollutants, reactive species such as $\cdot O_2^-$, h^+, and $\cdot OH$ play an important role in the photocatalytic process. To investigate the photocatalytic mechanism and better understand the performance of hollow Au−Cu_2O core−shell phtocatalysts, the effect of

DOI: 10.1021/acs.langmuir.6b00331
Langmuir 2016, 32, 3085−3094

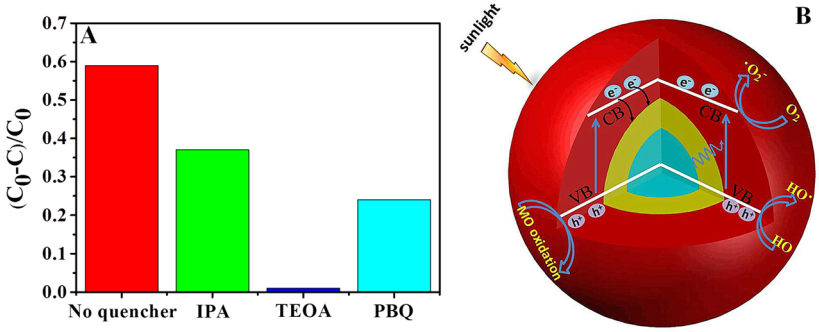

Figure 9. (A) Trapping experiment of active species during the photodegradation of MO in the presence of hollow Au−Cu_2O core−shell photocatalysts and different scavengers, such as triethanolamine (TEOA) as h^+ scavenger, isopropanol (IPA) as ·OH scavenger, and *p*-benzoquinone (PBQ) as $\cdot O_2^-$ scavenger, under visible-light irradiation for 1 h. The degradation percentage $(C_0 - C)/C_0$ is calculated by measuring the absorption of MO solution at each irradiation time interval (C) and the absorption of the initial concentration (C_0) at adsorption−desorption equilibrium. The HGN575 is used as the core, and the Cu_2O-shell thickness is about 28 nm. The structure-directing agent is PVP. (B) Schematic illustration of the generation and transfer of electron−hole pairs in the hollow Au−Cu_2O core−shell nanoparticles under visible-light irradiation.

scavengers on the MO degradation is examined to clarify the contribution of different reactive species during photocatalysis. As displayed in Figure 9A (HGN575 core, Cu_2O 28 nm, PVP as structure-directing agent), the addition of TEOA inhibits the MO degradation completely after irradiation for 1 h, which implies that photogenerated holes h^+ are the most important reactive specie during MO degradation. In addition, the presence of PBQ as $\cdot O_2^-$ scavengers significantly decreases the MO photodegradation efficiency, and the addition of IPA as ·OH scavengers causes conspicuous photocatalytic decolorization of MO. The results illustrate that h^+ and $\cdot O_2^-$ are the main reactive species for hollow Au−Cu_2O core−shell nanoparticles in the photocatalytic process. The drastic enhancement in photocatalytic activity may be ascribed to the synergistic effects of HGN cores and Cu_2O shells induced by the Schottky barrier and PIRET (Figure 9B). First, the Schottky barrier formed at the Au−Cu_2O interface which could act as an electron sink to capture and transfer photoexcited electrons from the Cu_2O nanoshells to the HGNs, reduce the carrier recombination, and increase the hole lifetime under solar light irradiation due to the larger work function of gold compared to Cu_2O.[35] Second, the HGN cores may enhance the light absorption, trapping and scattering through a local field enhancement effect under visible-light irradiation. The near-field EM coupling between the LSPR dipole of HGNs and the interband transition dipole of Cu_2O causes PIRET, resulting in obvious charge separation in the Cu_2O shell.[28,29,34] The photoexcited electrons from Cu_2O are likely to move to the HGN cores, while holes migrate to the Cu_2O surface. The O_2 molecules in the solution obtain the photoexcited electrons on the gold surface and are reduced to reactive species $\cdot O_2^-$, which can degrade MO molecules via the multiple-electron reduction reactions. Moreover, the accumulated holes on the Cu_2O surface favor oxidation decomposition of MO molecules directly or by the formation of intermediate ·OH species (Figure 9B). That is, the accelerated separation of the photogenerated electron−hole pairs could lead to the significant enhancement of the photocatalytic activity of the hollow Au−Cu_2O core−shell structures. Therefore, our results suggest that hollow Au−Cu_2O core−shell nanoparticles are better visible-light plasmonic photocatalyst than pristine Cu_2O crystals and solid Au−Cu_2O ones for MO photogradation under the effects of Schottky barrier and PIRET mechanisms.

4. CONCLUSION

In summary, a robust wet chemistry approach was employed to room-temperature synthesize hollow Au−Cu_2O core−shell nanoparticles for controllable regulation and enhancement of plasmonic properties of HGN cores via the dielectric Cu_2O nanoshells. The controllability over several important geometrical parameters, such as HGN core sizes, Cu_2O shell thicknesses, and morphologies related to structure-directing agents, allowed us to systematically and selectively fine-tune the synergistic extinction properties of the particles over a broad spectral range across the visible and near-infrared regions. Furthermore, the FDTD method was performed to theoretically interpret the geometry-dependent optical tunability of the hollow Au−Cu_2O core−shell nanoparticles. The simulated extinction spectra agreed well with the experimental ones, verifying the validity of our synthetic method in precise regulation for geometry-dependent optical properties. The hollow Au−Cu_2O core−shell nanoparticles exhibited enhanced photocatalytic activity for MO photodegradation under visible-light irradiation when compared to the pristine HGNs, Cu_2O, and solid Au−Cu_2O core−shell nanoparticles under the effects of Schottky barrier and PIRET mechanisms, announcing the great promise of the hollow core−shell nanoparticles with optimized synergetic performances for photonic, electronic, optoelectronic, and photocatalytic applications.

■ ASSOCIATED CONTENT

Supporting Information

The Supporting Information is available free of charge on the ACS Publications website at DOI: 10.1021/acs.langmuir.6b00331.

Extinction spectra and corresponding photographs of HGN and SGN colloids; TEM images and size distribution histograms of HGNs and SGNs; SEM images, TEM images, XRD patterns, and extinction spectra of pristine Cu_2O nanoparticles and solid Au−Cu_2O core−shell nanoparticles; extinction spectra of hollow Au−Cu_2O core−shell nanoparticles; extinction spectra of MO solution in the presence of different photocatalysts under visible-light irradiation (PDF)

DOI: 10.1021/acs.langmuir.6b00331
Langmuir 2016, 32, 3085−3094

AUTHOR INFORMATION

Corresponding Author

*(A.L.) E-mail liuaiping1979@gmail.com; phone +86 571 86843574.

Notes

The authors declare no competing financial interest.

ACKNOWLEDGMENTS

This work was supported by the National Natural Science Foundation of China (Nos. 51272237, 51175472, 11372280, and 11472191), the Zhejiang Provincial Natural Science Foundation of China (No. LY16E020011), the 521 Talent Project of Zhejiang Sci-Tech University, the Program for Innovative Research Team of Zhejiang Sci-Tech University, and the Opening Fund of State Key Laboratory of Nonlinear Mechanics.

REFERENCES

(1) Atwater, H. A.; Polman, A. Plasmonics for Improved Photovoltaic Devices. *Nat. Mater.* **2010**, *9*, 205−213.

(2) Costi, R.; Saunders, A. E.; Banin, U. Colloidal Hybrid Nanostructures: A New Type of Functional Materials. *Angew. Chem., Int. Ed.* **2010**, *49*, 4878−4897.

(3) Mokari, T.; Rothenberg, E.; Popov, I.; Costi, R.; Banin, U. Selective Growth of Metal Tips Onto Semiconductor Quantum Rods and Tetrapods. *Science* **2004**, *304*, 1787−1790.

(4) Zhang, L.; Jing, H.; Boisvert, G.; He, J. Z.; Wang, H. Geometry Control and Optical Tunability of Metal-Cuprous Oxide Core−Shell Nanoparticles. *ACS Nano* **2012**, *6*, 3514−3527.

(5) Sugawa, K.; Tahara, H.; Yamashita, A.; Otsuki, J.; Sagara, T.; Harumoto, T.; Yanagida, S. Refractive Index Susceptibility of the Plasmonic Palladium Nanoparticle: Potential as the Third Plasmonic Sensing Material. *ACS Nano* **2015**, *9*, 1895−1904.

(6) Sun, S. D. Recent advances in hybrid Cu_2O-based heterogeneous nanostructures. *Nanoscale* **2015**, *7*, 10850−10882.

(7) Jiang, R. B.; Li, B. X.; Fang, C. H.; Wang, J. F. Metal/Semiconductor Hybrid Nanostructures for Plasmon-Enhanced Applications. *Adv. Mater.* **2014**, *26*, 5274−5309.

(8) Yang, Y. C.; Wang, H. J.; Whang, J.; Huang, J. S.; Lyu, L. M.; Lin, P. H.; Gwo, S.; Huang, M. H. Facet-Dependent Optical Properties of Polyhedral Au−Cu_2O Core−Shell Nanocrystals. *Nanoscale* **2014**, *6*, 4316−4324.

(9) Li, G. D.; Tang, Z. Y. Noble Metal Nanoparticle@Metal Oxide Core/Yolk−Shell Nanostructures as Catalysts: Recent Progress and Perspective. *Nanoscale* **2014**, *6*, 3995−4011.

(10) Clavero, C. Plasmon-Induced Hot-Electron Generation at Nanoparticle/Metal-Oxide Interfaces for Photovoltaic and Photocatalytic Devices. *Nat. Photonics* **2014**, *8*, 95−103.

(11) Liz-Marzán, L. M.; Giersig, M.; Mulvaney, P. Synthesis of Nanosized Gold-Silica Core-Shell Particles. *Langmuir* **1996**, *12*, 4329−4335.

(12) Qi, J.; Chen, J.; Li, G.; Li, S.; Gao, Y.; Tang, Z. Facile Synthesis of Core−Shell Au@CeO_2 Nanocomposites with Remarkably Enhanced Catalytic Activity for CO Oxidation. *Energy Environ. Sci.* **2012**, *5*, 8937−8941.

(13) Majhi, S. M.; Rai, P.; Raj, S.; Chon, B.; Park, K.; Yu, Y. Effect of Au Nanorods on Potential Barrier Modulation in Morphologically Controlled Au@Cu_2O Core−Shell Nanoreactors for Gas Sensor Applications. *ACS Appl. Mater. Interfaces* **2014**, *6*, 7491−7497.

(14) Jiang, D.; Zhou, W.; Zhong, X.; Zhang, Y.; Li, X. Distinguishing Localized Surface Plasmon Resonance and Schottky Junction of Au−Cu_2O Composites by their Molecular Spacer Dependence. *ACS Appl. Mater. Interfaces* **2014**, *6*, 10958−10962.

(15) Hsu, S. C.; Liu, S. Y.; Wang, H. J.; Huang, M. H. Facet-Dependent Surface Plasmon Resonance Properties of Au−Cu_2O Core−Shell Nanocubes, Octahedra, and Rhombic Dodecahedra. *Small* **2015**, *11*, 195−201.

(16) Shi, X.; Ji, Y.; Hou, S.; Liu, W.; Zhang, H.; Wen, T.; Yan, J.; Song, M.; Hu, Z.; Wu, X. Plasmon Enhancement Effect in Au Gold Nanorods@Cu_2O Core−Shell Nanostructures and their Use in Probing Defect States. *Langmuir* **2015**, *31*, 1537−1546.

(17) Jing, H.; Large, N.; Zhang, Q.; Wang, H. Epitaxial Growth of Cu_2O on Ag Allows for Fine Control Over Particle Geometries and Optical Properties of Ag−Cu_2O Core−Shell Nanoparticles. *J. Phys. Chem. C* **2014**, *118*, 19948−19963.

(18) Liu, W.; Miroshnichenko, A. E.; Neshev, D. N.; Kivshar, Y. S. Broadband Unidirectional Scattering by Magneto-Electric Core−Shell Nanoparticles. *ACS Nano* **2012**, *6*, 5489−5497.

(19) Tyagi, H.; Mohapatra, J.; Kushwaha, A.; Aslam, M. Tuning the Observability of Surface Plasmon in Silica-Gold Raspberry Shaped Nanoparticles Using Cuprous Oxide Shell. *ACS Appl. Mater. Interfaces* **2013**, *5*, 12268−12274.

(20) Seh, Z. W.; Liu, S.; Low, M.; Zhang, S. Y.; Liu, Z.; Mlayah, A.; Han, M. Y. Janus Au−TiO_2 Photocatalysts with Strong Localization of Plasmonic Near-Fields for Efficient Visible-Light Hydrogen Generation. *Adv. Mater.* **2012**, *24*, 2310−2314.

(21) Bian, J. C.; Yang, F.; Li, Z.; Zeng, J. L.; Zhang, X. W.; Chen, Z. D.; Tan, J. Z. Y.; Peng, R. Q.; He, H. Y.; Wang, J. Mechanisms in Photoluminescence Enhancement of ZnO Nanorod Arrays by the Localized Surface Plasmons of Ag Nanoparticles. *Appl. Surf. Sci.* **2012**, *258*, 8548−8551.

(22) Liang, S.; Liu, X. L.; Yang, Y. Z.; Wang, Y. L.; Wang, J. H.; Yang, Z. J.; Wang, L. B.; Jia, S. F.; Yu, X. F.; Zhou, L. Symmetric and Asymmetric Au−AgCdSe Hybrid Nanorods. *Nano Lett.* **2012**, *12*, 5281−5286.

(23) Tan, C. S.; Hsu, S. C.; Ke, W. H.; Chen, L. J.; Huang, M. H. Facet-Dependent Electrical Conductivity Properties of Cu_2O Crystals. *Nano Lett.* **2015**, *15*, 2155−2160.

(24) Kuo, C. H.; Yang, Y. C.; Gwo, S.; Huang, M. H. Facet-Dependent and Au Nanocrystal-Enhanced Electrical and Photocatalytic Properties of Au−Cu_2O Core− Shell Heterostructures. *J. Am. Chem. Soc.* **2011**, *133*, 1052−1057.

(25) Oener, S. Z.; Mann, S. A.; Sciacca, B.; Sfiligoj, C.; Hoang, J.; Garnett, E. C. Au-Cu_2O Core−Shell Nanowire Photovoltaics. *Appl. Phys. Lett.* **2015**, *106*, 023501.

(26) Chang, S.; Li, Q.; Xiao, X.; Wong, K. Y.; Chen, T. Enhancement of Low Energy Sunlight Harvesting in Dye-Sensitized Solar Cells Using Plasmonic Gold Nanorods. *Energy Environ. Sci.* **2012**, *5*, 9444−9448.

(27) Bai, L.; Li, M.; Guo, K.; Luoshan, M.; Mehnane, H. F.; Pei, L.; Pan, M.; Liao, L.; Zhao, X. Plasmonic Enhancement of the Performance of Dye-Sensitized Solar Cell by Core−Shell AuNRs@SiO_2 in Composite Photoanode. *J. Power Sources* **2014**, *272*, 1100−1105.

(28) Ren, S.; Wang, B.; Zhang, H.; Ding, P.; Wang, Q. Sandwiched ZnO@Au@Cu_2O Nanorod Films as Efficient Visible-Light-Driven Plasmonic Photocatalysts. *ACS Appl. Mater. Interfaces* **2015**, *7*, 4066−4074.

(29) Li, J.; Cushing, S. K.; Bright, J.; Meng, F.; Senty, T. R.; Zheng, P.; Bristow, A. D.; Wu, N. Ag@Cu_2O Core-Shell Nanoparticles as Visible-Light Plasmonic Photocatalysts. *ACS Catal.* **2013**, *3*, 47−51.

(30) Zhang, N.; Liu, S.; Fu, X.; Xu, Y. Synthesis of M@TiO_2 (M= Au, Pd, Pt) Core−Shell Nanocomposites with Tunable Photoreactivity. *J. Phys. Chem. C* **2011**, *115*, 9136−9145.

(31) Rai, P.; Khan, R.; Raj, S.; Majhi, S. M.; Park, K. K.; Yu, Y. T.; Lee, I. H.; Sekhar, P. K. Au@Cu_2O Core−Shell Nanoparticles as Chemiresistors for Gas Sensor Applications: Effect of Potential Barrier Modulation On the Sensing Performance. *Nanoscale* **2014**, *6*, 581−588.

(32) Lin, Y. K.; Chiang, Y. J.; Hsu, Y. J. Metal−Cu_2O Core−Shell Nanocrystals for Gas Sensing Applications: Effect of Metal Composition. *Sens. Actuators, B* **2014**, *204*, 190−196.

(33) Cushing, S. K.; Li, J.; Meng, F.; Senty, T. R.; Suri, S.; Zhi, M.; Li, M.; Bristow, A. D.; Wu, N. Photocatalytic Activity Enhanced by Plasmonic Resonant Energy Transfer From Metal to Semiconductor. *J. Am. Chem. Soc.* **2012**, *134*, 15033−15041.

DOI: 10.1021/acs.langmuir.6b00331
Langmuir 2016, 32, 3085−3094

(34) Xiong, J.; Li, Z.; Chen, J.; Zhang, S.; Wang, L.; Dou, S. Facile Synthesis of Highly Efficient One-Dimensional Plasmonic Photocatalysts through Ag@Cu_2O Core−Shell Heteronanowires. *ACS Appl. Mater. Interfaces* **2014**, *6*, 15716−15725.
(35) Mahmoud, M. A.; Qian, W.; El-Sayed, M. A. Following Charge Separation On the Nanoscale in Cu_2O−Au Nanoframe Hollow Nanoparticles. *Nano Lett.* **2011**, *11*, 3285−3289.
(36) Wang, W. C.; Lyu, L. M.; Huang, M. H. Investigation of the Effects of Polyhedral Gold Nanocrystal Morphology and Facets On the Formation of Au−Cu_2O Core−Shell Heterostructures. *Chem. Mater.* **2011**, *23*, 2677−2684.
(37) Pan, Y. L.; Deng, S. Z.; Polavarapu, P.; Gao, N. Y.; Yuan, P. Y.; Sow, C. H.; Xu, Q. H. Plasmon-enhanced photocatalytic properties of Cu_2O nanowire−Au nanoparticle assemblies. *Langmuir* **2012**, *28*, 12304−12310.
(38) Wang, P.; Huang, B.; Dai, Y.; Whangbo, M. H. Plasmonic Photocatalysts: Harvesting Visible Light with Noble Metal Nanoparticles. *Phys. Chem. Chem. Phys.* **2012**, *14*, 9813−9825.
(39) Han, L.; Zhu, C.; Hu, P.; Dong, S. One-Pot Synthesis of a Au@TiO_2 Core−Shell Nanocomposite and its Catalytic Property. *RSC Adv.* **2013**, *3*, 12568−12570.
(40) Kong, L.; Chen, W.; Ma, D.; Yang, Y.; Liu, S.; Huang, S. Size Control of Au@ Cu_2O Octahedra for Excellent Photocatalytic Performance. *J. Mater. Chem.* **2012**, *22*, 719−724.
(41) Liu, D. Y.; Ding, S. Y.; Lin, H. X.; Liu, B. J.; Ye, Z. Z.; Fan, F. R.; Ren, B.; Tian, Z. Q. Distinctive Enhanced and Tunable Plasmon Resonant Absorption From Controllable Au@Cu_2O Nanoparticles: Experimental and Theoretical Modeling. *J. Phys. Chem. C* **2012**, *116*, 4477−4483.
(42) Fang, C.; Jia, H.; Chang, S.; Ruan, Q.; Wang, P.; Chen, T.; Wang, J. Gold Core)/(Titania Shell) Nanostructures for Plasmon-Enhanced Photon Harvesting and Generation of Reactive Oxygen Species. *Energy Environ. Sci.* **2014**, *7*, 3431−3438.
(43) Zhang, L.; Blom, D. A.; Wang, H. Au−Cu_2O Core−Shell Nanoparticles: A Hybrid Metal-Semiconductor Heteronanostructure with Geometrically Tunable Optical Properties. *Chem. Mater.* **2011**, *23*, 4587−4598.
(44) Li, B.; Gu, T.; Ming, T.; Wang, J.; Wang, P.; Wang, J.; Yu, J. C. Gold Core)@(Ceria Shell) Nanostructures for Plasmon-Enhanced Catalytic Reactions Under Visible Light. *ACS Nano* **2014**, *8*, 8152−8162.
(45) Li, P.; Wei, Z.; Wu, T.; Peng, Q.; Li, Y. Au−ZnO Hybrid Nanopyramids and their Photocatalytic Properties. *J. Am. Chem. Soc.* **2011**, *133*, 5660−5663.
(46) Kuo, C. H.; Hua, T. E.; Huang, M. H. Au Nanocrystal-Directed Growth of Au−Cu_2O Core−Shell Heterostructures with Precise Morphological Control. *J. Am. Chem. Soc.* **2009**, *131*, 17871−17878.
(47) Meir, N.; Jen-La Plante, I.; Flomin, K.; Chockler, E.; Moshofsky, B.; Diab, M.; Volokh, M.; Mokari, T. Studying the Chemical, Optical and Catalytic Properties of Noble Metal (Pt, Pd, Ag, Au)−Cu_2O Core−Shell Nanostructures Grown Via a General Approach. *J. Mater. Chem. A* **2013**, *1*, 1763−1769.
(48) Wang, H. J.; Yang, K. H.; Hsu, S. C.; Huang, M. H. Photothermal effects from Au−Cu_2O core−shell nanocubes, octahedra, and nanobars with broad near-infrared absorption tunability. *Nanoscale* **2016**, *8*, 965−972.
(49) Rej, S.; Wang, H. J.; Huang, M. X.; Hsu, S. C.; Tan, C. S.; Lin, F. C.; Huang, J. S.; Huang, M. H. Facet-dependent optical properties of Pd−Cu_2O core−shell nanocubes and octahedra. *Nanoscale* **2015**, *7*, 11135−11141.
(50) Huang, M. H.; Rej, S.; Chiu, C. Y. Facet-Dependent Optical Properties Revealed through Investigation of Polyhedral Au−Cu_2O and Bimetallic Core−Shell Nanocrystals. *Small* **2015**, *11*, 2716−2726.
(51) Talley, C. E.; Jackson, J. B.; Oubre, C.; Grady, N. K.; Hollars, C. W.; Lane, S. M.; Huser, T. R.; Nordlander, P.; Halas, N. J. Surface-Enhanced Raman Scattering From Individual Au Nanoparticles and Nanoparticle Dimer Substrates. *Nano Lett.* **2005**, *5*, 1569−1574.
(52) Chandra, M.; Dowgiallo, A. M.; Knappenberger, K. L., Jr. Controlled Plasmon Resonance Properties of Hollow Gold Nanosphere Aggregates. *J. Am. Chem. Soc.* **2010**, *132*, 15782−15789.
(53) Schwartzberg, A. M.; Olson, T. Y.; Talley, C. E.; Zhang, J. Z. Synthesis, Characterization, and Tunable Optical Properties of Hollow Gold Nanospheres. *J. Phys. Chem. B* **2006**, *110*, 19935−19944.
(54) Gong, X.; Tang, J.; Ji, Y.; Wu, B.; Wu, H.; Liu, A. Adjustable Plasmonic Optical Properties of Hollow Gold Nanospheres Monolayers and LSPR-dependent Surface-Enhanced Raman Scattering of Hollow Gold Nanosphere/Graphene Oxide Hybrids. *RSC Adv.* **2015**, *5*, 42653−42662.
(55) Palik, E. D. *Handbook of Optical Constants of Solids I*; Academic Press: San Diego, CA, 1985; Vol. *1*.
(56) Palik, E. D. *Handbook of Optical Constants of Solids II*; Academic Press: Waltham, MA, 1991; Vol. *3*.
(57) Sun, Z.; Yang, Z.; Zhou, J.; Yeung, M. H.; Ni, W.; Wu, H.; Wang, J. A General Approach to the Synthesis of Gold-Metal Sulfide Core−Shell and Heterostructures. *Angew. Chem., Int. Ed.* **2009**, *48*, 2881−2885.
(58) Zhang, J.; Tang, Y.; Lee, K.; Ouyang, M. Nonepitaxial Growth of Hybrid Core-Shell Nanostructures with Large Lattice Mismatches. *Science* **2010**, *327*, 1634−1638.
(59) Christopher, P.; Ingram, D. B.; Linic, S. Enhancing Photochemical Activity of Semiconductor Nanoparticles with Optically Active Ag Nanostructures: Photochemistry Mediated by Ag Surface Plasmons. *J. Phys. Chem. C* **2010**, *114*, 9173−9177.

DOI: 10.1021/acs.langmuir.6b00331
Langmuir 2016, 32, 3085−3094